Elastic reflection waveform inversion with petrophysical model constraints

Daniel Rocha & Paul Sava, Center for Wave Phenomena, Colorado School of Mines

SUMMARY

Elastic wavefield tomography faces challenging pitfalls due to its multiparameter and multicomponent character, while seeking a model that generates accurate and high-quality images of the subsurface. Inter-parameter crosstalk and absence of petrophysical constraints cause elastic inversion to fail, delivering unphysical and artifact-contaminated models. Therefore, we propose to use the elastic reflection waveform inversion (ERWI) methodology, which inverts both for the background velocity model and for the reflectivity image, coupled with a petrophysical constraint term. We demonstrate that constraining ERWI leads to models that are more plausible, exhibit fewer artifacts, and obey the imposed constraints. We alternate between smooth and rough model updates, keeping both data fitting, image focusing and petrophysical constraints consistent with one another in a common objective function. Compared to unconstrained inversion, our method delivers a higher-quality model as well as improved convergence and accuracy.

INTRODUCTION

Wavefield tomography provides high-resolution velocity estimation by accurate wave extrapolation using the full waveform and bandwidth of seismic signals. Its implementations are classified as either data-domain, i.e., full-waveform inversion (FWI) (Lailly, 1983; Tarantola, 1984) and/or as image-domain, i.e., wave-equation migration velocity analysis (WEMVA) (Sava and Biondi, 2004; Symes, 2008; Yang and Sava, 2011; Diaz et al., 2013). However, FWI might fail and not deliver models that improve image quality since it suffers from cycle skipping and does not explicitly constrain the migrated images. Also, this technique is more suitable for diving and direct waves, although reflections dominate surface data and migrated images. Alternatively, WEMVA seeks the model that delivers the most focused image, but such model is generally deficient in high resolution.

As a mixed-domain wavefield tomography method, reflection waveform inversion (RWI) has recently gained interest by using reflections in data-domain wavefield tomography and also inverting for the migrated image (Hicks and Pratt, 2001; Xu et al., 2012; Wang et al., 2013; Guo and Alkhalifah, 2017). This technique exploits an objective function in the data domain and separately updates the smooth and rough (i.e., image) parts of the earth model, such that the smooth model only incorporates low-wavenumber updates. Least-squares migration robustly computes the rough model (Alves and Biondi, 2016; Feng and Schuster, 2017; Duan et al., 2017), while optimization via adjoint-state method provides the smooth updates (Tarantola, 1988; Sava, 2014).

For all wavefield tomography methods, a multiparameter earth model via elastic extrapolation delivers more realistic reflectivity and valuable subsurface information (Chang and McMechan, 1987; Yan and Sava, 2011; Ravasi and Curtis, 2013). However, multiparameter inversion suffers from crosstalk among model parameters (Operto et al., 2013; Pan and Innanen, 2016). Coupling between the multiple wave modes and their different illumination responses cause contamination of the inverted model. Radiation pattern analysis clarifies the ambiguity among physical properties (Burridge et al., 1998; Köhn et al., 2012; Kamath and Tsvankin, 2016; Oh and Alkhalifah, 2016), but also shows that amplitude responses overlap for different earth model contrasts, thus expressing the difficulty to isolate sensitivity kernels for the various parameters, especially with limited acquisition coverage and highly irregular illumination.

To mitigate the inter-parameter crosstalk and thus obtain a more geological-plausible model, various authors propose using known physical relationships between parameters to constrain the elastic inversion (Baumstein, 2013; Peters et al., 2015; Duan and Sava, 2016). This methodology delivers more realistic models since crosstalk and artifacts do not obey petrophysical properties. We choose to impose such physical constraints on the earth model and implement a scheme that simultaneously optimizes the model and the migrated image. Our petrophysical model constraint uses a logarithmic barrier similarly to the method by Duan and Sava (2016), but applied in the context of mixed-domain elastic wavefield tomography. Therefore, our method avoids the combined harmful effect of inter-parameter crosstalk (by physical constraints) and high-wavenumber updates (by low-wavenumber RWI gradients) into the inversion.

THEORY

We consider the elastic wave equation

$$\rho\ddot{\mathbf{u}} - \nabla\left[\lambda\left(\nabla\cdot\mathbf{u}\right)\right] - \nabla\cdot\left[\mu\left(\nabla\mathbf{u}+\nabla\mathbf{u}^{\mathrm{T}}\right)\right] = \mathbf{f}\ , \quad (1)$$

where $\mathbf{u}\left(\mathbf{x},t\right)$ is the wavefield, $\mathbf{f}\left(\mathbf{x},t\right)$ is the source, $\lambda\left(\mathbf{x}\right)$ and $\mu\left(\mathbf{x}\right)$ are Lamé parameters, $\rho\left(\mathbf{x}\right)$ is the density of the medium, ∇ represents spatial derivative operators, and the superscript dot indicates time differentiation. Under the single-scattering assumption, one can consider both wavefield and medium parameters as composed of a background and a small perturbation:

$$\rho = \rho_0 + \delta\rho\ , \lambda = \lambda_0 + \delta\lambda\ , \mu = \mu_0 + \delta\mu\ , \quad (2)$$

$$\mathbf{u} = \mathbf{u}_0 + \delta\mathbf{u}\ , \quad (3)$$

where δ indicates small perturbed quantities, and the subscript $_0$ indicates background quantities. Substituting equations 2-3 in equation 1, and ignoring higher-order terms involving the product of the small earth

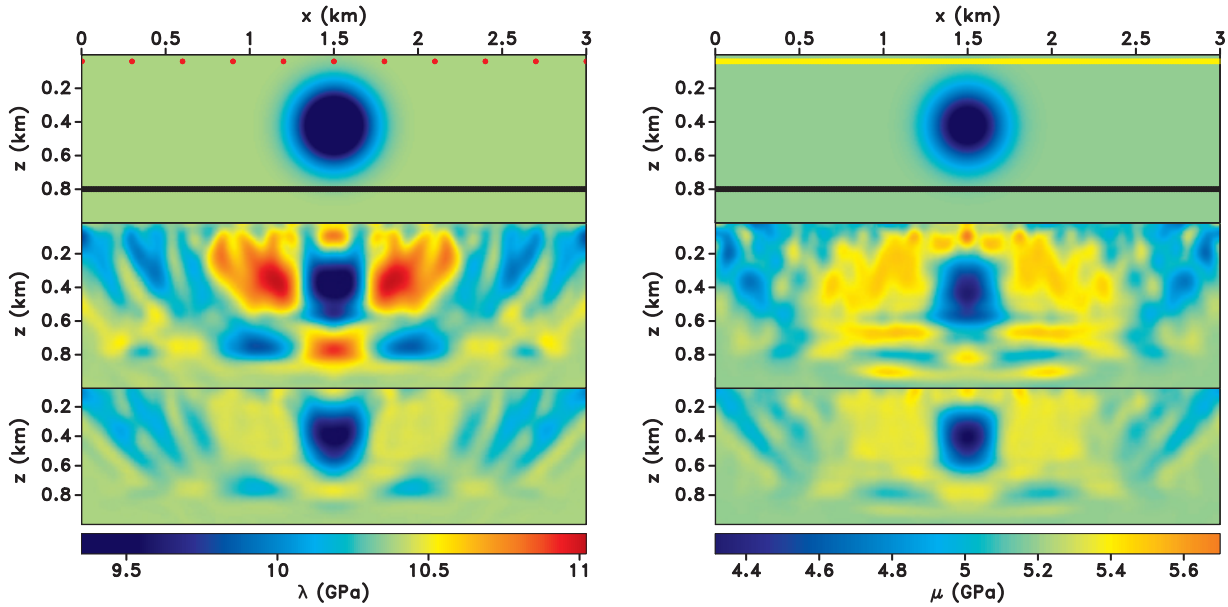

Figure 1: True (top), unconstrained (middle), and constrained (bottom) inverted models for (a) λ and (b) μ. The top panels also show the 11 sources (red) and the line of multicomponent receivers (yellow), and the reflector (black). Adding the physical constraint term into the inversion mitigates the spurious artifacts from inter-parameter crosstalk and sparse acquisition, delivering a more plausible earth model.

model perturbations with $\delta\mathbf{u}$, we obtain

$$\rho_0\delta\ddot{\mathbf{u}}-\nabla[\lambda_0(\nabla\cdot\delta\mathbf{u})]-\nabla\cdot\Big[\mu_0\Big(\nabla\delta\mathbf{u}+\nabla\delta\mathbf{u}^{\mathrm{T}}\Big)\Big]= \quad (4)$$
$$-\delta\rho\ddot{\mathbf{u}}_0+\nabla[\delta\lambda(\nabla\cdot\mathbf{u}_0)]+\nabla\cdot\Big[\delta\mu\Big(\nabla\mathbf{u}_0+\nabla\mathbf{u}_0^{\mathrm{T}}\Big)\Big]+\mathbf{f}.$$

Equation 4 indicates the interaction between model perturbations $(\delta\rho, \delta\lambda, \delta\mu)$ and the background wavefield $\mathbf{u}_0$ in the source term for the scattered wavefield $\delta\mathbf{u}$, which leads to the scattered data $\delta\mathbf{d} = \mathbf{K}_r\delta\mathbf{u}$ ($\mathbf{K}_r$ is an extraction operator at receivers). Therefore, we write the model perturbations generating scattered data as

$$\delta\mathbf{d} = \mathbf{K}_r\delta\mathbf{u} = \mathbf{L}\delta\mathbf{m}\ , \quad (5)$$

where $\delta\mathbf{m} = [\delta\rho\ \ \delta\lambda\ \ \delta\mu]^{\mathrm{T}}$ and $\mathbf{L}$ is the single-scattering operator, whose adjoint is migration:

$$\delta\mathbf{m}_{mig} = \mathbf{L}^{\mathrm{T}}\delta\mathbf{d}\ . \quad (6)$$

Least-squares migration leads to a more robust $\delta\mathbf{m}$ image by minimizing the following objective function

$$\mathcal{J}_{LS} = \frac{1}{2}\|\mathbf{L}\delta\mathbf{m} - \delta\mathbf{d}\|^2\ . \quad (7)$$

Using $\mathbf{L}$ and $\mathbf{L}^{\mathrm{T}}$, one minimizes equation 7 by

$$\delta\mathbf{m}_{LS} = \left(\mathbf{L}^{\mathrm{T}}\mathbf{L}\right)^{-1}\mathbf{L}^{\mathrm{T}}\delta\mathbf{d}\ . \quad (8)$$

Equation 8 describes the least-squares inversion of the model perturbation $\delta\mathbf{m}$, while keeping the background model $\mathbf{m}_0 = [\rho_0\ \ \lambda_0\ \ \mu_0]^{\mathrm{T}}$ unchanged. To update $\mathbf{m}_0$, we perform non-linear inversion based on the adjoint-state method, which formulates equation 1 as

$$\mathbf{A}(\mathbf{m})\mathbf{u} = \mathbf{f}\ , \quad (9)$$

where $\mathbf{A}(\mathbf{m})$ is the elastic wave-equation operator and $\mathbf{m}$ represents the total model. For data-misfit minimization, the objective function for total model inversion is

$$\mathcal{J}_D = \frac{1}{2}\|\mathbf{d} - \mathbf{d}_{obs}\|^2 = \frac{1}{2}\|\mathbf{K}_r\mathbf{u} - \mathbf{d}_{obs}\|^2\ , \quad (10)$$

where $\mathbf{d}_{obs}$ is observed data. To construct the model update, the gradient of $\mathcal{J}_D$ with respect to $\mathbf{m}$ is

$$\frac{\partial\mathcal{J}_D}{\partial\mathbf{m}} = \frac{\partial\mathbf{A}}{\partial\mathbf{m}}\mathbf{u}\star\mathbf{a}\ , \quad (11)$$

where $\frac{\partial\mathbf{A}}{\partial\mathbf{m}}$ involves derivatives applied to the state wavefield (Tarantola, 1984; Plessix, 2006). The symbol $\star$ in equation 11 represents zero-lag crosscorrelation between the state ($\mathbf{u}$) and adjoint ($\mathbf{a}$) wavefields. The adjoint wavefield uses the adjoint wave-equation operator and the objective function derivative with respect to the state wavefield as its source term:

$$\mathbf{A}^{\mathrm{T}}(\mathbf{m})\mathbf{a} = \frac{\partial\mathcal{J}_D}{\partial\mathbf{u}} = \mathbf{K}_r^{\mathrm{T}}\left(\mathbf{d} - \mathbf{d}_{obs}\right)\ . \quad (12)$$

Conventional FWI uses the gradient expression in equation 11. Alternatively, in RWI, both state and adjoint wavefields are decomposed into background and scattered parts based on equation 3:

$$\frac{\partial\mathcal{J}_D}{\partial\mathbf{m}} = \frac{\partial\mathbf{A}}{\partial\mathbf{m}}\left(\mathbf{u}_0 + \delta\mathbf{u}\right)\star\left(\mathbf{a}_0 + \delta\mathbf{a}\right)\ , \quad (13)$$

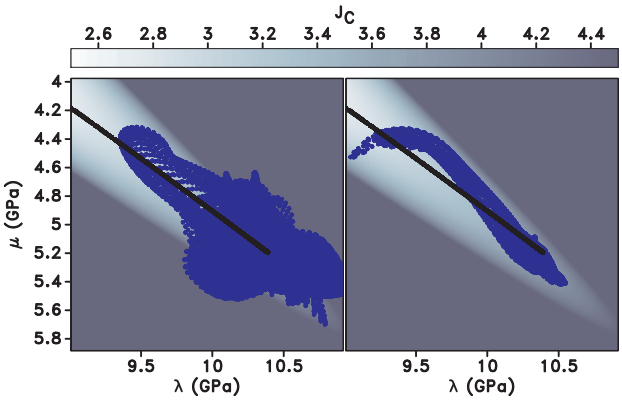

Figure 2: Crossplot in λ-μ space of inverted models: unconstrained (left) and constrained (right). The black line corresponds to the true model. The logarithmic barrier function used in the constrained inversion is plotted in the background. The unconstrained inverted model is spread throughout the model space without following a trend, while the constrained model is restricted to the region delimited by the barriers.

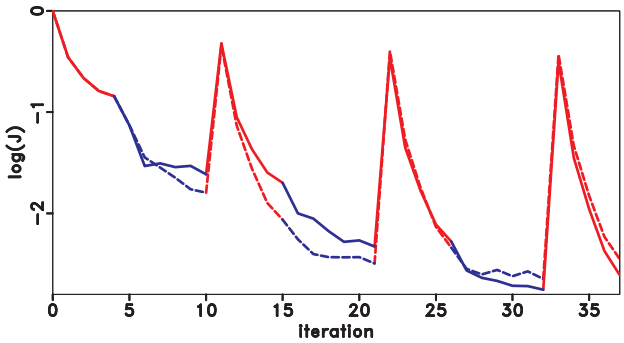

Figure 3: Objective functions in logarithmic scale for unconstrained (dashed) and constrained (solid) ERWIs, which alternate between least-squares migration of model perturbations (red) and waveform inversion of background model (blue). Note how constrained ERWI performs better at the final iterations for both smooth model (at iteration 32) and image (final) inversions.

which leads to

$$\frac{\partial \mathcal{J}_D}{\partial \mathbf{m}} = \frac{\partial \mathbf{A}}{\partial \mathbf{m}} \left[\mathbf{u}_0 \star \delta\mathbf{a} + \delta\mathbf{u} \star \mathbf{a}_0 + \mathbf{u}_0 \star \mathbf{a}_0 + \delta\mathbf{u} \star \delta\mathbf{a} \right] . \tag{14}$$

The separation between background and scattered wavefields provides low-wavenumber content for the waveform inversion gradient. The first term in equation 14 involves crosscorrelation of waves propagating from the source to the image point, while the second correlates waves propagating from the receivers to the image point. Hence, such events coincide in space and time along their similar propagation paths, resulting in low wavenumbers. The other two terms involve crosscorrelation of waves that only coincide at the image point, producing reflectivity that is characterized by high wavenumbers. Therefore, RWI provides the smooth update ($\mathbf{m}_0$) by

$$\frac{\partial \mathcal{J}_D}{\partial \mathbf{m}_0} = \frac{\partial \mathbf{A}}{\partial \mathbf{m}} \left[\mathbf{u}_0 \star \delta\mathbf{a} + \delta\mathbf{u} \star \mathbf{a}_0 \right] . \tag{15}$$

Auxiliary terms in the objective function that act in the model space avoids inversion results with unphysical models, which are common with data-only objection functions. For instance, one can exploit known physical relationships between two sets of model parameters by a logarithmic penalty function (Peng et al., 2002; Gasso et al., 2009; Duan and Sava, 2016):

$$\mathcal{J}_C = -\eta \sum_{\mathbf{x}} \left[\log(h_u) + \log(h_l) \right] , \tag{16}$$

where η is a weighting scalar parameter relative to the other objective function terms, while h_u and h_l define functions in the dual-model space determining its upper and lower bounds, which for λ and μ are

$$h_u = -\lambda + c_u\mu + b_u = 0 , \qquad h_l = \lambda - c_l\mu - b_l = 0 , \tag{17}$$

where $c_{u,l}$ and $b_{u,l}$ are the slopes and intercepts of the lines. For model pairs that fall inside the region bounded by h_u and h_l, the distance to the barrier lines determines the value of the constraint. Model samples that are close to one of the barrier lines during inversion lead to large $\mathcal{J}_C$, and are thus forced to move away from that barrier.

The gradient of $\mathcal{J}_C$ with respect to either λ or μ is

$$\frac{\partial \mathcal{J}_C}{\partial \lambda} = \frac{-\eta}{\lambda - c_u\mu - bu} - \frac{\eta}{\lambda - c_l\mu - bl} , \tag{18}$$

$$\frac{\partial \mathcal{J}_C}{\partial \mu} = \frac{\eta c_u}{\lambda - c_u\mu - bu} + \frac{\eta c_l}{\lambda - c_l\mu - bl} . \tag{19}$$

Equations 18 and 19 show that the gradient tends to ∞ if any of its denominators tends to 0. The total objective function involving data-misfit term and petrophysical constraint is

$$\mathcal{J} = \mathcal{J}_D + \mathcal{J}_C . \tag{20}$$

EXAMPLE

We illustrate our ERWI method with the synthetic elastic model shown in Figure 1, where the top of Figures 1a and 1b show the acquisition geometry, the reflector location and the negative Gaussian anomalies for the true λ and μ models, respectively. We use as initial model the constant background from the true model. After 38 inversion iterations, which alternate between smooth and rough model updates, we obtain the models with unconstrained (middle of Figure 1) and constrained (bottom of Figure 1) ERWIs. Note how the constrained ERWI mitigates the spurious artifacts around the anomaly in the unconstrained inverted model, which are caused by a combination of sparse geometry, limited bandwidth and crosstalk between model parameters. The constraint term uses two barrier lines defined by $h_l = \lambda - 1.5\mu - 1.98$ and $h_u = -\lambda + \mu + 5.43$ according to equation 17. The background of Figure 2 shows a map of $\mathcal{J}_C$ with two

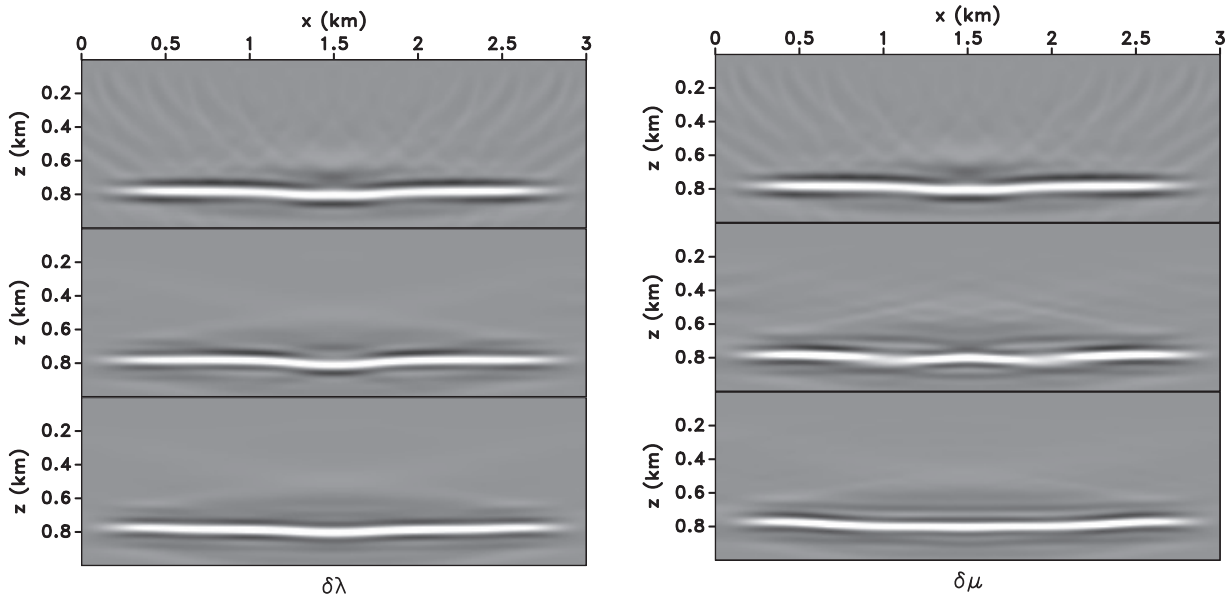

(a) (b)

Figure 4: RTM (top) and LSRTM (middle) images obtained with the initial velocity, and LSRTM (bottom) images obtained with constrained inverted velocities for (a) $\delta\lambda$ and (b) $\delta\mu$. Note the sparse acquisition artifacts in RTM, the irregularity of the imaged flat reflector for RTM and LSRTM as imprint of wrong velocity, and the improved reflector flatness and focusing for LSRTM with the constrained inverted velocity.

visible convergent barrier lines, and all model samples from unconstrained and constrained inversions. The unconstrained model samples are spread broadly into the model space, while the constrained samples are confined within the barriers and closer to the line of true model samples. The point in this line that is closest to the bottom-right corner is the background model value, where both constrained and unconstrained inversions start from. Both ERWIs alternate between image (rough model) and background (smooth model) inversions, and their objective functions decrease over iterations, as shown in Figure 3. The unconstrained inversion has a smaller objective function for the first 20 iterations. However, for the remaining iterations, the constrained ERWI has better performance for the objective function, finalizing with smaller residuals for both smooth and rough model inversions relatively to the unconstrained ERWI.

To show how ERWI with physical constraints delivers a model that effectively increases image quality, we show the model perturbation $\delta\lambda$ and $\delta\mu$ images in Figures 4a and 4b, respectively. The top reverse time migration (RTM) images show the cross-cutting artifacts due to sparse acquisition and a false subsidence of the flat reflector due to imaging with the wrong initial velocity. Performing least-squares migration (LSRTM) with the initial inversion background model provides image improvement (middle images in Figure 4) by mitigating the cross-cutting artifacts and sharpening the imaged reflector, but still exhibits the imprint of the wrong velocity at the center of the reflector for $\delta\lambda$, and at $[x, z] = [1, 0.8]$ km and $[x, z] = [2, 0.8]$ km for $\delta\mu$. Finally, using the constrained ERWI model, LSRTM delivers the bottom images in Figure 4, which show a flatter reflector closer to the true one.

CONCLUSIONS

We use the mixed-domain ERWI framework coupled with petrophysical constraints to seek both high-quality images and plausible earth models. Smooth updates are possible for the background model by implementing separation of wavefields into their background and scattered constituents, whose proper correlation provides low-wavenumber gradients. Our model constraints are based on a linear trend between two model parameters, impeding the inversion to deliver an unphysical model with crosstalk artifacts. Although our constrained ERWI method has an additional objective function term based on the imposed constraints, we achieve improved convergence compared to conventional data-misfit minimization.

ACKNOWLEDGEMENTS

We thank the sponsors of the Center for Wave Phenomena, whose support made this research possible. The synthetic examples in this paper use the Madagascar open-source software package (Fomel et al., 2013) freely available from http://www.ahay.org.